PHILOSOPHICAL TRANSACTIONS B

rstb.royalsocietypublishing.org

Research

**Cite this article:** Knutsen PM, Mateo C, Kleinfeld D. 2016 Precision mapping of the vibrissa representation within murine primary somatosensory cortex. *Phil. Trans. R. Soc. B* **371**: 20150351.
http://dx.doi.org/10.1098/rstb.2015.0351

Accepted: 11 July 2016

One contribution of 15 to a Theo Murphy meeting issue 'Interpreting BOLD: a dialogue between cognitive and cellular neuroscience'.

**Subject Areas:**
neuroscience

**Keywords:**
blood oxygen level-dependent (BOLD) imaging, functional imaging, intrinsic optical signal, vibrissa, whisker

**Author for correspondence:**
David Kleinfeld
e-mail: dk@physics.ucsd.edu

THE ROYAL SOCIETY PUBLISHING

# Precision mapping of the vibrissa representation within murine primary somatosensory cortex

Per M. Knutsen[1], Celine Mateo[1] and David Kleinfeld[1,2,3]

[1]Department of Physics, [2]Section of Neurobiology, and [3]Department of Electrical and Computer Engineering, UC San Diego, La Jolla, CA, USA

DK, 0000-0001-9797-4722

The ability to form an accurate map of sensory input to the brain is an essential aspect of interpreting functional brain signals. Here, we consider the somatotopic map of vibrissa-based touch in the primary somatosensory (vS1) cortex of mice. The vibrissae are represented by a Manhattan-like grid of columnar structures that are separated by inter-digitating septa. The development, dynamics and plasticity of this organization is widely used as a model system. Yet, the exact anatomical position of this organization within the vS1 cortex varies between individual mice. Targeting of a particular column *in vivo* therefore requires prior mapping of the activated cortical region, for instance by imaging the evoked intrinsic optical signal (eIOS) during vibrissa stimulation. Here, we describe a procedure for constructing a complete somatotopic map of the vibrissa representation in the vS1 cortex using eIOS. This enables precise targeting of individual cortical columns. We found, using C57BL/6 mice, that although the precise location of the columnar field varies between animals, the relative spatial arrangement of the columns is highly preserved. This finding enables us to construct a canonical somatotopic map of the vibrissae in the vS1 cortex. In particular, the position of any column, in absolute anatomical coordinates, can be established with near certainty when the functional representations in the vS1 cortex for as few as two vibrissae have been mapped with eIOS.

This article is part of the themed issue 'Interpreting BOLD: a dialogue between cognitive and cellular neuroscience'.

## 1. Introduction

The body surface is topographically represented point-for-point in the somatosensory cortex. This somatotopic organization is particularly striking in the case of the long mystacial sinus hairs, or vibrissae, in rodents. Here, each vibrissa is represented in the primary somatosensory (vS1) cortex by a column of neurons that responds exclusively to some aspect of motion of that hair. The columns for different vibrissa are arranged in a Manhattan-like lattice that matches the spatial distribution of vibrissae in the mystacial pad [1]; reviewed in [2]. This special geometry is historically referred to as the 'barrel field' and has enabled studies that depend on the contrasting effect of manipulating one sensory input, or vibrissa, relative to control conditions for neighbouring vibrissae. As examples, these include neuronal development and plasticity [3–7], electrical dynamics among neighbouring columns [8–14], the transference of learning between columns [15], microstrokes to single columns [16] and local blood-flow dynamics [17,18]. Further studies involve multi-columnar reconstructions of neuron architectonics [19–21] and large-scale neural network simulations [21].

The detailed location of cortical columns within the vS1 cortex varies between animals [22]. Thus, measurements to ascertain the precise spatial geometry of the vibrissa field are necessary when measurements, stimulation or injections in specific columns are required. A common and non-invasive

method to map the vibrissa field is to image the evoked intrinsic optical signal (eIOS) [23–25] through a cranial window [26] or thinned transcranial window [27,28]. The eIOS, like the blood oxygen level-dependent (BOLD) functional magnetic resonant image (fMRI) signal [29,30], exploits the change in electronic structure of haemoglobin that occurs when heme transitions from the oxidized to reduced, or deoxygenated, state [31]. This transition results in a change in the absorption spectrum [23,32]. Thus a wavelength of the light can be selected to predominantly measure either a relative increase or decrease in blood oxygen concentration [33,34]; the absorption at so-called 'isobestic points' are sensitive only to the total concentration of haemoglobin. Concurrent with the change in absorption is a change in the magnetic state of haemoglobin. Oxyhaemoglobin is weakly diamagnetic while deoxyhaemoglobin is a strong paramagnet; the later state leads to a gradient in the local magnetic field of blood vessels and may be detected via dephasing of the magnetization of water protons.

Here, we focus on mapping with the eIOS and consider single wavelength measurements in the relatively broad near infrared range of 620–780 nm, where the absorption of deoxyhaemoglobin exceeds that of oxyhaemoglobin. Thus an increase in metabolism leads to an increase of absorption and a concurrent decrease in the reflectance of light. In response to vibrissa stimulation, the eIOS follows a triphasic time course [35]. Relative to the pre-stimulus light reflectance, the eIOS is initiated by a brief, approximately 1 s net-negative reflectance, historically labelled the 'initial dip', followed by 1–2 s net-positive reflectance and concluded by a prolonged, i.e. 5 s or longer net-negative reflectance. The initial net-negative phase of the eIOS is presumed to reflect oxygen consumption as a result of heightened neural activity, while the following net-positive phase results from an active vasodynamic response that increases the diameter of vessels within the activated cortical column, as measured optically [36,37] and by fMRI [38]. While the initial deoxygenation related component co-localizes closely with the activated cortical column, the vasodynamic response may not [35,39]. This limits the precision of eIOS, and by inference BOLD fMRI, in mapping studies.

Early studies that used eIOS to map the representation of individual vibrissae in the vS1 cortex were limited to mapping between five and nine vibrissae in the same animal [40–42]. More recently, we described a protocol, motivated by the prescient fMRI work of Kim and co-workers [43], for mapping of the entire vibrissae field during isoflurane anaesthesia [17]. We used this protocol to demonstrate that eIOS maps are precisely co-localized with the anatomically described vibrissa columns [17]. Anaesthesia generally suppresses the amplitude of haemodynamic responses [44–52]. Strong vasodilators such as isoflurane [43,53], however, specifically suppress the vasodynamic component and isolate the localized haemodynamic eIOS component that is caused by tissue deoxygenation, i.e. the build-up of deoxyhaemoglobin. This leads to improved signal-to-noise in eIOS images [17,54,55]. Here, we describe further improvements in the technique of eIOS mapping under isoflurane and generate complete maps of the vibrissa field across a large cohort of C57BL/6 mice. We use this data to complete a canonical map of the vibrissa field, along with the variability in that map.

## 2. Material and methods

### (a) Subjects

Twenty-nine female C57BL/6 Thy1-ChR2 transgenic mice (JAX strain B6.Cg-Tg(Thy1-COP4/EYFP)18Gfng/J) [56], of 22–24 g in mass and ages 5–18 weeks, were prepared for intrinsic optical imaging; the presence of channelrhodopsin is not relevant for this work and relates to subsequent manipulations performed with these animals. The weight range of these mice was similar to that reported for wild-type female C57BL/6 mice [57].

### (b) Surgery

Each animal was anaesthetized with 1.5–2.0% isoflurane (v/v) in oxygen, and maintained at a constant body temperature of 37°C using a temperature control system (no. 40–90–8; FHC Inc.). The bone overlying the vS1 cortex was thinned [28]. Briefly, the bone was skim-cut with a drill (EXL-M40, Osada, CA, USA) and a no. 005 bit (Hager & Meisinger GmbH) past the cancellous layer to a final thickness of no more than 100 µm. Two to four fiducial marks were painted close to the corners of the thinned-skull window with a fine-point black ink pen (Sakura, Pigma Micron 005, Japan). The coordinates of the fiducial marks were measured relative to bregma with a stereotactic device with an accuracy of about 10 µm. The bone was left to air-dry and covered with a thin layer of cyanoacrylate glue over which a piece of #0 cover glass was placed. The edges of the window were covered with dental cement (Grip Cement, Denstply #675571) and a custom made titanium-alloy head-bar attached for head-fixation during imaging experiments. The mice were given analgesics (Buprenex, Reckitt Benckiser Pharmaceuticals; 7 µg per mouse) at the conclusion of surgery.

### (c) Intrinsic optical signal imaging

During imaging sessions, animals were either awake or anaesthetized with isoflurane at 1.8–2.0% (v/v) in oxygen. Imaging with acclimated and head-fixed mice was performed as described and illustrated [36,58]. Anaesthetized mice were maintained at a constant body temperature of 37°C using a temperature control system (no. 40–90–8; FHC Inc.) and continuously infused with 5% (v/v) glucose in 0.9% (w/v) NaCl subcutaneously at a rate of 10 ml $kg^{-1}$ $h^{-1}$ using a syringe pump (no. 780101; Harvard Apparatus), as previously described [17]. Awake mice were administered 5% (v/v) glucose in water orally before and after imaging sessions. Imaging experiments in anaesthetized animals lasted 3–5 h.

We followed previously described protocols for intrinsic optical imaging [17,24]. Briefly, a pair of front-to-front camera lenses imaged an approximately 4 × 4 mm region on the cortical surface onto a 512 × 512 pixel region of a CCD camera (Pantera TF 1M60; Teledyne Dalsa) at a resolution of 7.87 µm per pixel. Prior to eIOS imaging, a reference vessel image was recorded with illumination at 455 nm (no. M455L2; ThorLabs). Throughout functional imaging, the cortical surface was illuminated at 625 nm (no. M625L2; Thorlabs). Frames were acquired as averages over 0.5 s intervals using a custom-written LabView application (National Instruments, Austin, TX, USA). For activation of the cortical representation of the vibrissae, individual vibrissae were trimmed to 70–90% of their full length, placed inside a quartz capillary attached to a piezoelectric element, and displaced 0.5 mm in both rostral and caudal directions with a 10 Hz sinusoidal pattern for 4 s at a distance of 10% of the original length. Four seconds of baseline activity was acquired prior to stimulation, 4 s during stimulation, and 16 s after the end of stimulus, for a total of 24 s of data per trial. The inter-trial interval was 10 s. Five to thirty trials were acquired and averaged per vibrissa; the exact number was

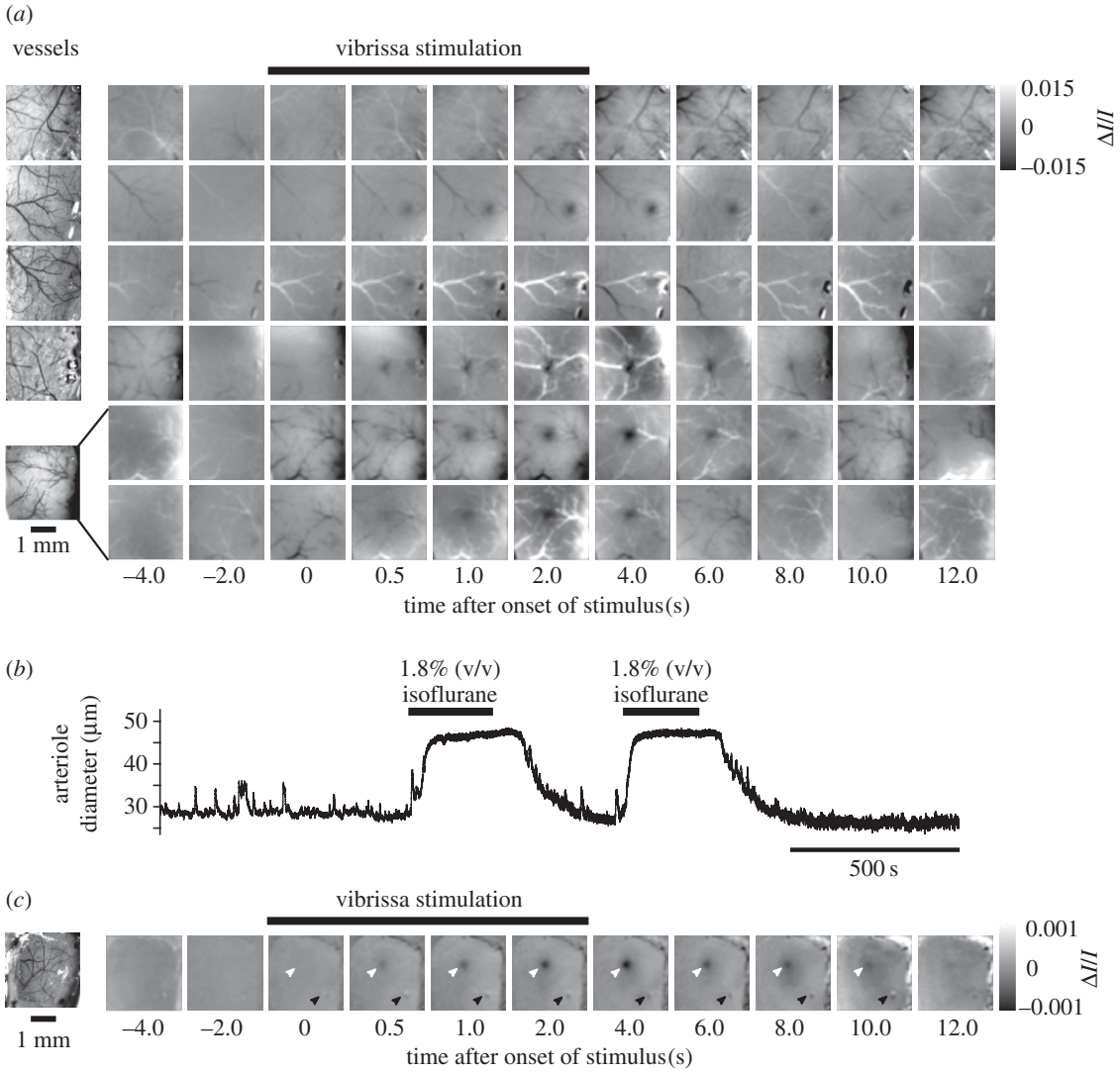


**Figure 1.** (*a*) Evoked IOS measured in the vS1 cortex of awake, head-fixed mice during stimulation of the C2 vibrissa. Time points indicate the onset of 0.5 s frames. The images in each row are the average across 20 sequential trials. The data in the top five rows are from different animals while that in the sixth row is a second set of trials from the same animal and field as used for the fifth row. The left-most images were taken under 455 nm illumination and show the layout of dural and pial vessels. (*b*) Vasodilatory effects of isoflurane on pial arteriole diameter measured in an awake, head-fixed mouse transitioning in and out of anaesthetized state induced by administration of 1.8% (v/v) isoflurane. (*c*) Intrinsic optical signals measured in an isoflurane anaesthetized mouse before, during and after stimulation of the C4 vibrissa; 20 trial average. White arrows point to the region of evoked activity. Black arrows point to the location of a motion artefact rendering a fiducial on the bone under the window visible in the signal images.

decided by inspecting the data on-the-fly. This procedure was repeated for 12–30 vibrissae in the same animal. A total of 635 vibrissae were mapped across 28 different mice.

## (d) Image analysis

Raw image frames were loaded into MATLAB (MathWorks, Natick, MA, USA) and processed with custom-written code. A single baseline image ($R_{base}$) was created by averaging over eight, 0.5 s frames that preceded stimulus onset. Signal frames ($\Delta I_f/I_f$) were generated by subtracting and normalizing individual frames ($R_f$) by this baseline using the formula $\Delta I_f/I_f = (R_f - R_{base})/R_{base}$ [59]. The median pixel value across the entire field was subtracted from all pixels of each signal frame to balance the effects of large, spontaneous fluctuations caused by isoflurane induced burst suppression [60]. Finally, we averaged each frame across multiple trials.

Maps of the entire field of the macro-vibrissae in the vS1 cortex were computed as follows (figures 1–4):

1. The stimulus-evoked map of a single-vibrissa's cortical representation was generated by averaging signal frames in the range 0.5–5.0 s after stimulus onset (figure 1*c*). This procedure was repeated for all vibrissa mapped in the same mouse.
2. Individual vibrissa maps were cropped by a circular region of interest, 0.5–1.5 mm in diameter ($0.90 \pm 0.22$ mm; mean $\pm$ s.d.), that was manually centred on the evoked region. This was necessary because of an occasional presence of motion artefacts, associated in particular with the edges of the imaging windows and fiducial marks on bone under the window. Motion artefacts were readily distinguished from evoked activity by their dark-bright appearance (figure 1*c*).
3. Vibrissae maps were next convolved with a $0.25 \times 0.25$ mm Gaussian window with width $\sigma = 0.08$ mm.
4. Vibrissa maps were normalized and thresholded at 20% of the maximum signal amplitude.
5. All vibrissae maps obtained from the same animal were combined by taking the maximum value, pixel by pixel, across all maps. With one exception (figure 4*c*), this maximum projection was computed before any spatial transformations (figure 3).

The location and orientation of an eIOS map combined from many single-vibrissa maps was found from fiducial marks placed on the bone outside the thinned part of the imaging window during surgery. These marks, which had known

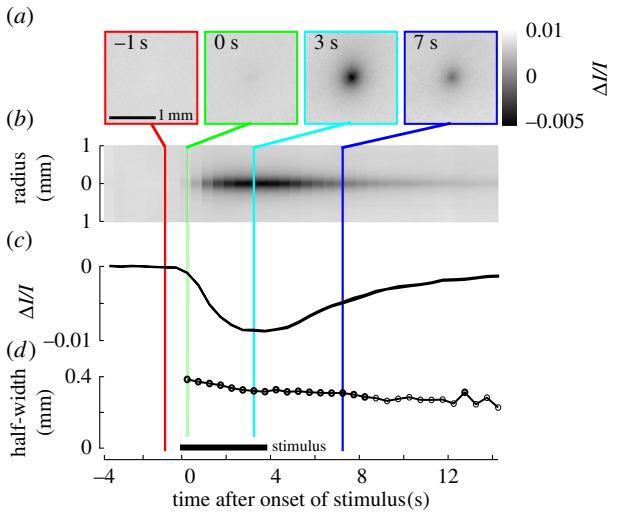


**Figure 2.** Evoked IOSs measured in isoflurane anaesthetized mice. We averaged across a subset of 268 vibrissae, whose eIOS centroids were located within the centre 2 × 2 mm region in images. (*a*) Evoked IOS maps obtained during single-vibrissa stimulation, centred and averaged at different time points relative to stimulation onset. Each frame is the average eIOS over 0.5 s. (*b*) Average eIOS maps collapsed and averaged in all radial directions, illustrating the spatial extent and time course of the eIOS. The panel is mirror symmetric with respect to the horizontal axis. The crossing coloured lines correspond to the time points of frames in panel (*a*). (*c*) Average amplitude of the eIOS as a function of time, measured at the negative peak. The trace fluctuates in thickness corresponding to its standard error. (*d*) Half-width of the eIOS as a function of time.

anatomical coordinates relative to bregma, were manually selected in images taken with illumination at 455 nm (figure 1*c*). The pair of fiducial marks with the largest spatial separation was used to compute the location of bregma, in units of pixels, and to align an anatomical grid onto the acquired frames. All eIOS maps were then rotated and reflected such that the medio-lateral and rostro-caudal axes were coincident with the abscissa and ordinate, respectively (figure 3).

The relative organization of the vibrissa field across mice was compared by aligning all combined eIOS maps with the map that contained the largest number of mapped vibrissae (figure 3*a*), as follows:

1. For each vibrissa eIOS map the pixel coordinate of the peak amplitude was obtained, yielding a set of control coordinates with known vibrissae IDs for each animal. The set of coordinates obtained in the reference animal are referred to as the 'reference coordinates'.
2. For each set of control coordinates, vibrissae ID and coordinates that did not exist in the reference set were removed.
3. The 'control coordinates' were then spatially registered with the reference coordinates, based on vibrissae IDs, through a least-squares affine transformation optimization routine using the 'cp2tform' function in the MATLAB Image Processing Toolbox. We used the 'similarity' transformation type that includes rotation, scaling, translation and reflection.

A canonical vibrissa representation in the vS1 cortex was obtained by averaging all maps across mice, as follows:

1. For each unique vibrissa, e.g. C2, the pixel coordinate of the peak eIOS amplitude was obtained across all animals, yielding a spatial distribution of eIOS peak-amplitude locations in absolute anatomical coordinates with a mean and standard deviation (figure 4*a*). A new reference set of vibrissa representation coordinates was defined as the set of mean peak-amplitude locations, across animals.
2. Each set of control coordinates, as defined above, was then spatially registered to this new reference set of average coordinates in absolute anatomical coordinates. This transformation resulted in a data structure containing the spatial transformation.
3. The spatial transformation was then applied to the each of the individual maps of the raw eIOS, averaged for the 0.5–5 s time-span after stimulation onset. The spatially transformed maps were next averaged by vibrissa ID across all animals, yielding an average eIOS map in absolute anatomical coordinates per vibrissa.
4. Each average eIOS map was then normalized and thresholded at 20% of the maximum amplitude, as described above, before the maximum projection was computed across all vibrissae. This maximum projection map resulted in what we term a 'canonical map' of the vibrissa representation in the vS1 cortex (figure 4*c*). Additional statistics of this canonical map were computed, such as the half-width (figure 4*d*) and average locations of individual vibrissa representations (table 1).

### (e) Single vessel imaging

The effect of isoflurane on vasodynamics of individual arterioles was ascertained with two-photon imaging of thinned-skull, head-fixed animals [58].

## 3. Results

Cortical activation during sensory stimulation is typically much stronger in awake compared with anaesthetized rodents [46]. Thus, we initially assessed the suitability of using an awake preparation for precise somatotopic mapping. We mechanically stimulated one vibrissa at a time at 10 Hz for 4 s [17]. In awake, head-fixed mice we found that the trial-to-trial variability in the eIOS measured with 625 nm illumination was generally high and persisted when comparing blocks of averaged trials (20 trials) (figure 1*a*). Although we were able to reproduce blocks of trials with tri-phasic response, these features were not seen in every block of averaged trials. In some blocks the 'initial dip' persisted for the duration of the stimulus. More generally, there was significant overlap in time and space between large amplitude vasodynamic responses and the smaller amplitude responses associated with direct neuronal activation by vibrissa stimulation. All told, the rich vasodynamics observed with eIOS in awake animals complicates its use as a tool to rapidly map individual columns in the vS1 cortex.

Isoflurane induces vasodilation of cortical blood vessels (figure 1*b*) via activation of ATP-sensitive $K^+$ channels [43,53] and thus suppresses the potential for vasodynamic events during somatosensory stimulation [17,54]. We found that intrinsic signals, void of vasodynamic signatures evoked by vibrotactile stimulation, could be obtained for up to 5 h when isoflurane anaesthesia was combined with thermal regulation and continuous subcutaneous administration of 5% (w/v) glucose in NaCl (figure 1*c*). This allowed us to precisely locate the somatotopic representation of each vibrissa, one-by-one, in the vS1 cortex. The exact concentration of isoflurane in oxygen was critical for this result. If the isoflurane level was too low, vasodynamic responses associated with vessels re-appeared even though the animal

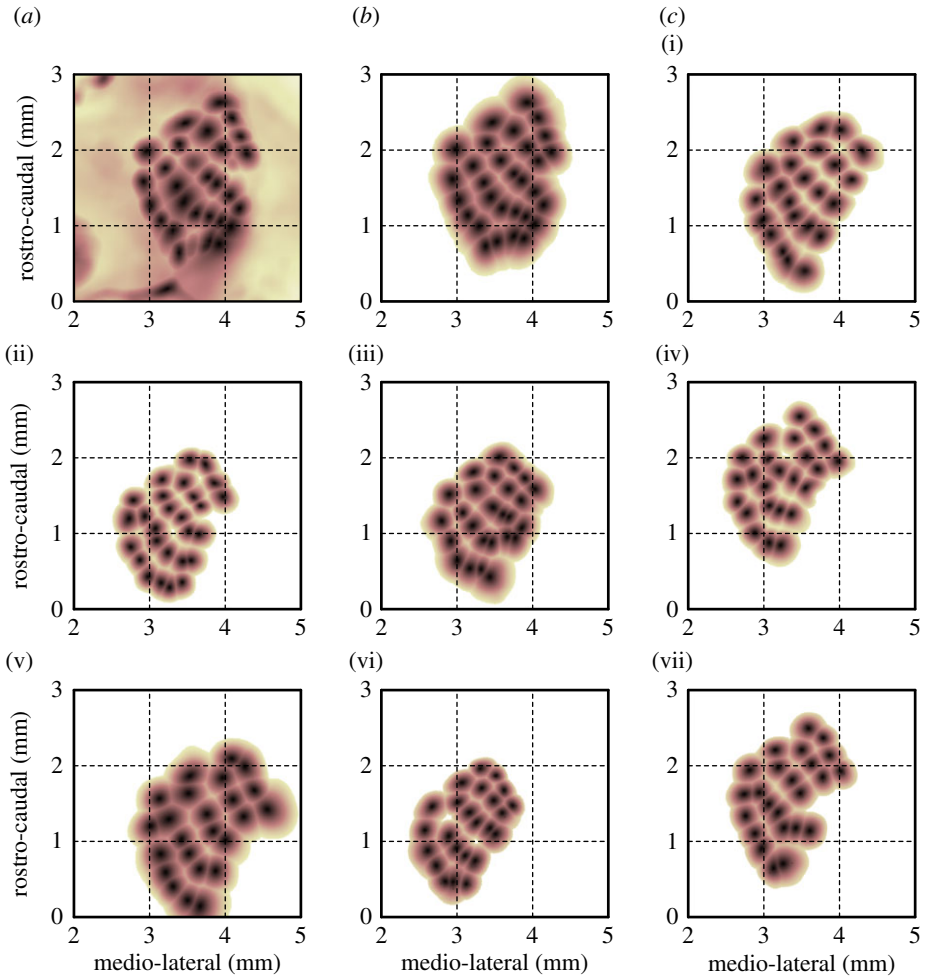


**Figure 3.** (*a*) Maximum projection of 30 single-vibrissa eIOS maps measures in the same mouse. The maps were normalized and smoothed ($\sigma = 80$ μm) prior to projection. (*b*) The same combined map as in panel (*a*), except that individual maps were first cropped by a circular ROI centred on the negative peak of the eIOS, then normalized and thresholded at 20%. This particular map served as the reference map for later alignment of maps across different mice. (*c*)(i–vii). Multi-vibrissa eIOS maps obtained from seven additional mice, pre-processed and projected as in panel (*b*).

remained anaesthetized. If the isoflurane level was too high, the amplitude of the eIOS was suppressed or not observed at all. An isoflurane level close to 1.8% (v/v) in oxygen overall provided the best results. The data in figure 2 shows the average evoked spatial signature and time course of the intrinsic signal before, during, and after a 4 s vibrotactile stimulus. The amplitude of the eIOS response grew throughout stimulation, peaked at about 4 s, and then receded to baseline beyond 10 s after stimulation ceased (figure 2*a–c*). The area, or half-width, of the evoked response decreased monotonically with time following stimulation onset (figure 2*d*). The half-width decreased faster during the 4 s stimulation period, at $-20.7$ μm s$^{-1}$, and slower after vibrissa stimulation ceased, at $-6.8$ μm s$^{-1}$.

The appearance of only a single feature in the eIOS response for each vibrissa enabled us to combine individual responses into a single somatotopic map (figure 3*a*) (Material and methods); we cropped the individual maps within a circle, if required, to remove movement or vasodynamic artefacts (figure 3*b*). The stereotypic layout of the vibrissae representation in the vS1 cortex was apparent in the combined somatotopic maps of all mapped mice; eight representative maps are shown in figure 3. The absolute location and orientation of the vibrissae map, however, varied between animals. The centroids of the eIOS clustered in anatomical coordinates according to the identity of mapped vibrissae (figure 4*a* and table 1). On average, across all mapped vibrissae, the standard deviation of eIOS centroids averaged by vibrissa identity (circles in figure 4*a*) was $0.31 \pm 0.04$ mm (mean ± s.d.), or approximately two columnar radii. By comparison, the average inter-row distance between nearest-neighbour eIOS centroids was $0.16 \pm 0.04$ mm (mean ± s.d.). Thus the absolute location of the vibrissae relative to the bregma point is quite variable between animals.

Qualitatively, the relative layout of the vibrissa representation in the vS1 cortex was well preserved across mice (figure 3). To quantify the relative configuration of the vibrissa representation across animals, the eIOS map from each mouse was aligned to a reference map, chosen as the map with the largest number of vibrissae (figure 3*b*). The alignment was solely through an affine transformation, found by least-squares optimization of distances to eIOS centroids in the reference map. The re-scaled and aligned maps, with respect to the reference map, are shown in figure 4*b*; the centroids of individual eIOS vibrissa maps have been colour coded according to vibrissa identity. In these relative coordinates, the eIOS centroids were more tightly clustered than in absolute coordinates. Averaged across all vibrissae, the standard deviation of centroid positions was $0.036 \pm 0.010$ mm (mean ± s.d.), as grouped by vibrissa identity, averaged across the horizontal and vertical axes (figure 4*b* and

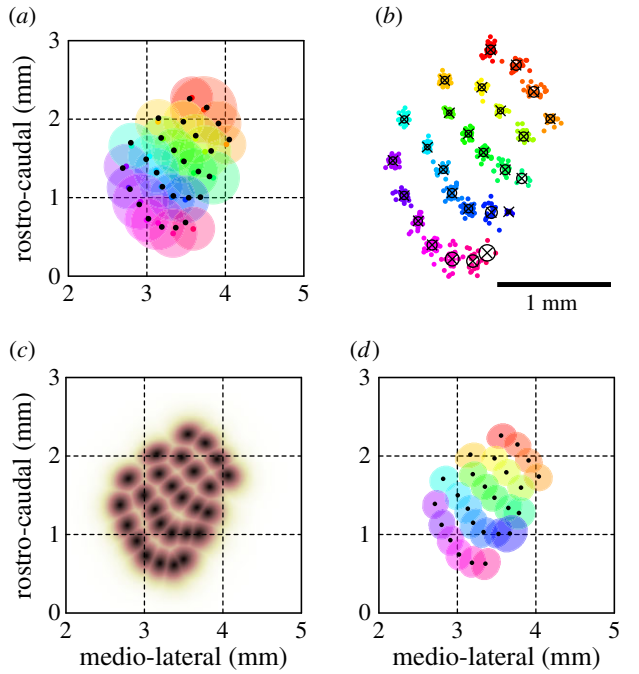


**Figure 4.** Construction of a canonical map in the vS1 cortex. (*a*) Distributions of eIOS centroids, in absolute anatomical coordinates, represented by the mean (black dots) and standard deviation (circles colour coded by vibrissa identity) of the geometric position of eIOS centroids (541 vibrissae from 25 mice). (*b*) Distributions of eIOS centroids, in relative anatomical coordinates (629 vibrissae from 28 mice). The locations of map centroids obtained from the same mouse were maintained in fixed relative coordinates and rotated, translated and re-scaled to optimally match, in the least-squared sense, the location, scale, and orientation of centroids of a reference eIOS map (figure 3*b*). Centroids of individual eIOS maps are plotted and colour coded by vibrissae identity (as in panel (*a*)), and additionally represented by the average (black x's) and standard deviations (black circles) of their relative geometric positions. (*c*) Canonical somatotopic map of the vibrissa representation in the vS1 cortex. Individual eIOS maps were aligned as in part (*b*) and then averaged, according to vibrissa identity, across all 28 mice and combined through normalization and maximal projection to yield an average map in relative coordinates. This map was then transformed to absolute coordinates by finding the affine transform (in the least-squares sense) that matched the distribution of eIOS centroids in relative coordinates (x's in in panel (*b*)) onto the distribution of eIOS centroids in absolute coordinates (black dots in in panel (*a*)). The result shown is thus the combined eIOS map of all individual vibrissa, averaged across mice, at its average spatial location and orientation in absolute anatomical coordinates relative to bregma. We term this map the canonical map of vibrissa representation in the vS1 cortex. (*d*) Spatial locations of individual vibrissa representations in the vS1 cortex in terms of the centroids and half-widths of the eIOS of the canonical vibrissa map.

table 1). Thus the relative spatial configuration of the somatotopic vibrissae eIOS map is highly stereotyped across mice (figure 4*b*).

Evoked eIOS responses during vibrissa stimulation are well co-localized with the position of the underlying columns but do not stop at the boundaries of these structures [17] (figure 2). Averaged across all vibrissae, the half-width of the eIOS (figure 3*d*) was $0.36 \pm 0.06$ mm (mean $\pm$ s.d.) (table 1), which is more than the average diameters of vibrissa columns in mice [17]. The eIOS thus extends into septa and neighbouring columns. Figure 4*d* shows the contours of where the eIOS for each vibrissa was greater than the half-maximal response. This measure is an approximation of the half-width, but also highlights the asymmetries and orientation of the eIOS, e.g. compare the eIOS orientation of straddlers versus row E vibrissae.

We now come to the construction of a *canonical somatotopic map* of the vibrissa representation in the vS1 cortex. The location of eIOS centroids, averaged by vibrissa identity, was spatially registered from relative (figure 4*b*) to absolute (figure 4*a*) coordinates, in the least-squares sense, by affine transformation. The same transformation was then applied to every individual vibrissa eIOS map obtained, and the transformed eIOS maps were averaged across mice by vibrissa identity, normalized, and used to compute the maximum projection across all vibrissae. In total, the canonical somatotopic vibrissa map (figure 4*d*) encompassed 27 macro-vibrissae across all rows and arcs, including all straddlers.

## 4. Discussion

We obtained a total of 635 *in vivo* maps, across 28 different mice, of the somatotopic representation of macro-vibrissa in the vS1 cortex using an improved method for imaging the eIOS [17]. We compared eIOS responses in awake and isoflurane anaesthetized mice (figure 1). Consistent with previous studies showing that isoflurane has vasodilatory properties [43,53], we observed strong dilation of pial arterioles when isoflurane was administered at 1.8% (v/v) in oxygen (figure 1*b*). Although we observed that isoflurane anaesthesia suppressed the amplitude of the eIOS (figure 1*a*,*c*), isoflurane improved the signal-to-noise of the eIOS deoxygenation signal by suppressing vasodynamic responses (figures 1*a*,*c* and 2). Beyond a dependence on the concentration of isoflurane in oxygen, high quality imaging depended on the maintenance of normal body temperature and the continuous subcutaneous injection of glucose.

We observed that in the absence of a large vasodynamic 'overshoot', the deoxyhaemoglobin signal persisted at the same location in cortex throughout the 4 s time window during vibrissa stimulation (figure 2). This result suggests that changes in blood flow and volume, such as that associated with sensory-induced dilation of cortical blood vessels [36], normally mask haemodynamic signals in the eIOS attributed to increased neural activity. The persistence of a deoxyhaemoglobin signal enabled us to average acquisition frames over the entire stimulation time window, thereby improving the spatial specificity of the eIOS method. Previous studies within BOLD fMRI have reported similar improved spatial specificity with the vasodilator sodium nitroprusside [61]. Lastly, it is possible that the maps may be further refined though optimization of the stimulus interval and duty cycle [39,41].

While the absolute location and orientation of the vibrissa field varied between animals (figure 4*a*), we found that the relative arrangement of the field was preserved across mice (figure 4*b*), consistent with previous studies in mice [62] and rats [63]. Spatial spreads of the centroids of cortical columns for the same vibrissa averaged 0.036 mm (s.d.), or approximately less than one-fifth of the average columnar radius [62] and less than a quarter of the average inter-column distance. Thus, the location of any vibrissa column can be established with near certainty in coordinates relative

**Table 1.** Location and spatial distribution of individual vibrissa intrinsic map peaks. ML: lateral distance of map peak relative to the horizontal midline passing through bregma point. RC: caudal distance of map peak relative to bregma. s.d.$^{rel}$: standard deviation of the spread of mapped eIOS centroids after affine transformation (cf. Figure 4*b*). s.d.$^{abs}$: standard deviation of the spread of mapped eIOS centroid in absolute coordinates (cf. Figure 4*a*). Half-width: width of the eIOS at 50% peak amplitude.

| vibrissa | ML (mm) | RC (mm) | s.d.$^{rel}$ (μm) | s.d.$^{abs}$ (μm) | half-width (μm) |
|---|---|---|---|---|---|
| $\alpha$ | 3.56 | 2.26 | 38 | 287 | 348 |
| $\beta$ | 3.16 | 2.02 | 30 | 324 | 354 |
| $\gamma$ | 2.81 | 3.48 | 27 | 329 | 350 |
| $\delta$ | 2.71 | 1.39 | 31 | 297 | 348 |
| A1 | 3.77 | 2.15 | 41 | 359 | 334 |
| A2 | 3.91 | 1.95 | 43 | 379 | 336 |
| A3 | 4.04 | 1.74 | 32 | 270 | 179 |
| B1 | 3.47 | 1.97 | 28 | 269 | 358 |
| B2 | 3.62 | 1.79 | 25 | 323 | 358 |
| B3 | 3.81 | 1.60 | 37 | 297 | 340 |
| C1 | 3.19 | 1.77 | 21 | 269 | 340 |
| C2 | 3.35 | 1.61 | 27 | 278 | 340 |
| C3 | 3.47 | 1.47 | 33 | 280 | 340 |
| C4 | 3.65 | 1.34 | 40 | 306 | 348 |
| C5 | 3.79 | 1.27 | 42 | 336 | 414 |
| D1 | 3.00 | 1.50 | 22 | 281 | 348 |
| D2 | 3.13 | 1.33 | 31 | 275 | 354 |
| D3 | 3.20 | 1.15 | 37 | 304 | 360 |
| D4 | 3.33 | 1.03 | 34 | 326 | 366 |
| D5 | 3.52 | 1.00 | 49 | 353 | 366 |
| D6 | 3.67 | 1.01 | 16 | 461 | 464 |
| E1 | 2.79 | 1.12 | 33 | 322 | 358 |
| E2 | 2.91 | 0.92 | 35 | 351 | 364 |
| E3 | 3.02 | 0.74 | 41 | 333 | 368 |
| E4 | 3.18 | 0.63 | 56 | 284 | 374 |
| E5 | 3.36 | 0.62 | 51 | 306 | 386 |
| E6 | 3.48 | 0.69 | 60 | 276 | 530 |

to all other columns. Assuming a flat vertical projection, as used in this study, eIOS imaging of two or few vibrissae in a novel mouse may be used to find the orientation and scale between the new vibrissa map and the canonical map (figure 4*c*). Alternative methods may also be used to locate individual vibrissa representations in vS1, such as extracellular recording. The canonical map is then either formed manually, using figure 4*b* as a template, or by computationally finding an affine transformation that minimizes the offsets between the measured columnar locations and the average locations provided in table 1. Thus our canonical map should increase the speed and precision of mapping procedures, in support of physiological investigations of the vibrissa system [2,64].

It will be of interest to determine whether the mean position and variability of the centroids and boundaries of other sensory maps in the cortex have as reproducible a map as that for the vibrissae. This includes the retinotopic organization of the multitude of visual areas [65,66] and the tonotopic versus periodotopic (harmonic) organization of the primary auditory cortex [67–69].

Ethics. All protocols were approved by the Institutional Animal Care and Use Committee at UCSD.

Authors' contributions. All authors planned the experiments. The data were obtained by P.M.K. and C.M., analysed by P.M.K., and the manuscript was written by P.M.K. and D.K. All reagents were contributed by D.K., who further attended to the myriad of university rules and forms that govern environmental health and safety, including the ethical use of animals as well as the use chemicals, controlled substances and hazardous substances.

Competing interests. We declare we have no competing interests.

Funding. Our work was supported by the United States National Institutes of Mental Health (grant no. MH108503), United States National Institutes of Biomedical Imaging and Bioengineering (grant no. EB003832), United States National Institutes of Neurological Disease and Stroke (grants nos. NS058668 and NS057198), and the United States National Science Foundation (grant no. PHY153264).

Acknowledgements. We thank Pablo Blinder, Patrick Drew and Michael Pesavento for contributions to code used for eIOS imaging and analysis.

## References


1. Woolsey TA, Van Der Loos H. 1970 The structural organization of layer IV in the somatosensory region (SI) of mouse cerebral cortex. *Brain Res*. **17**, 205–242. (doi:10.1016/0006-8993(70)90079-X)
2. Petersen CC. 2007 The functional organization of the barrel cortex. *Neuron* **56**, 339–355. (doi:10.1016/j.neuron.2007.09.017)
3. Simons DJ, Land PW. 1987 Early experience of tactile stimulation influences organization of somatic sensory cortex. *Nature* **326**, 694–697. (doi:10.1038/326694a0)
4. Fox K. 1992 A critical period for experience-dependent synaptic plasticity in rat barrel cortex. *J. Neurosci*. **12**, 1826–1838.
5. Polley DB, Kvasnak E, Frostig RD. 2004 Naturalistic experience transforms sensory maps in the adult cortex of caged animals. *Nature* **429**, 67–71. (doi:10.1038/nature02469)
6. Lendvai B, Stern EA, Chen B, Svoboda K. 2000 Experience-dependent plasticity of dendritic spines in the developing rat barrel cortex *in vivo*. *Nature* **404**, 876–881. (doi:10.1038/35009107)
7. Erzurumlu RS, Gaspar P. 2012 Development and critical period plasticity of the barrel cortex. *Eur. J. Neurosci*. **35**, 1540–1553. (doi:10.1111/j.1460-9568.2012.08075.x)
8. Simons DJ. 1985 Temporal and spatial integration in the rat SI vibrissa cortex. *J. Neurophysiol*. **54**, 615–635.
9. Mirabella G, Battiston S, Diamond ME. 2001 Integration of multiple-whisker inputs in rat somatosensory cortex. *Cereb. Cortex* **11**, 164–170. (doi:10.1093/cercor/11.2.164)
10. Armstrong-James M, Fox K. 1987 Spatiotemporal convergence and divergence in the rat S1 'barrel' cortex. *J. Comp. Neurol*. **263**, 265–281. (doi:10.1002/cne.902630209)
11. Armstrong-James M, Fox K, Das-Gupta A. 1992 Flow of excitability within barrel cortex on striking a single vibrissa. *J. Neurophysiol*. **68**, 1345–1358.
12. Frostig RD, Xiong Y, Chen-Bee CH, Kvasnák E, Stehberg J. 2008 Large-scale organization of rat sensorimotor cortex based on a motif of large activation spreads. *J. Neurosci*. **28**, 13 274–13 284. (doi:10.1523/JNEUROSCI.4074-08.2008)
13. Kleinfeld D, Delaney KR. 1996 Distributed representation of vibrissa movement in the upper layers of somatosensory cortex revealed with voltage sensitive dyes. *J. Comp. Neurol*. **375**, 89–108. (doi:10.1002/(SICI)1096-9861(19961104)375:1<89::AID-CNE6>3.0.CO;2-K)
14. Gentet LJ, Avermann M, Matyas F, Staiger JF, Petersen CCH. 2010 Membrane potential dynamics of GABAergic neurons in the barrel cortex of behaving mice. *Neuron* **65**, 422–435. (doi:10.1016/j.neuron.2010.01.006)
15. Harris JA, Diamond ME. 2000 Ipsilateral and contralateral transfer of tactile learning. *Neuroreport* **11**, 263–266. (doi:10.1097/00001756-200002070-00008)
16. Shih AY, Blinder P, Tsai PS, Friedman B, Stanley G, Lyden PD, Kleinfeld D. 2013 The smallest stroke: occlusion of one penetrating vessel leads to infarction and a cognitive deficit. *Nat. Neurosci*. **16**, 55–63. (doi:10.1038/nn.3278)
17. Blinder P, Tsai PS, Kaufhold JP, Knutsen PM, Suhl H, Kleinfeld D. 2013 The murine cortical angiome: an interconnected vascular network with noncolumnar patterns of blood flow. *Nat. Neurosci*. **16**, 889–897. (doi:10.1038/nn.3426)
18. Woolsey TA, Rovainen CM, Cox SB, Henger MH, Liange GE, Liu D, Moskalenko YE, Sui J, Wei L. 1996 Neuronal units linked to microvascular modules in cerebral cortex: response elements for imaging the brain. *Cereb. Cortex* **6**, 647–660. (doi:10.1093/cercor/6.5.647)
19. Helmstaedter M, de Kock CP, Feldmeyer D, Bruno RM, Sakmann B. 2007 Reconstruction of an average cortical column *in silico*. *Brain Res. Rev*. **55**, 193–203. (doi:10.1016/j.brainresrev.2007.07.011)
20. Narayanan RT, Egger R, Johnson AS, Mansvelder HD, Sakmann B, de Kock CP, Oberlaender M. 2015 Beyond columnar organization: cell type- and target layer-specific principles of horizontal axon projection patterns in rat vibrissal cortex. *Cereb. Cortex* **25**, 4450–4468. (doi:10.1093/cercor/bhv053)
21. Markram H *et al.* 2015 Reconstruction and simulation of neocortical microcircuitry. *Cell* **163**, 456–492. (doi:10.1016/j.cell.2015.09.029)
22. Strominger RN, Woolsey TA. 1987 Templates for locating the whisker area in fresh flattened mouse and rat cortex. *J. Neurosci. Methods* **22**, 113–118. (doi:10.1016/0165-0270(87)90004-5)
23. Frostig RD, Lieke EE, Ts'o DY, Grinvald A. 1990 Cortical functional architecture and local coupling between neuronal activity and the microcirculation revealed by *in vivo* high-resolution optical imaging of intrinsic signals. *Proc. Natl Acad. Sci. USA* **87**, 6082–6086. (doi:10.1073/pnas.87.16.6082)
24. Grinvald A, Lieke EE, Frostig RD, Gilbert CD, Wiesel TN. 1986 Functional architecture of cortex revealed by optical imaging of intrinsic signals. *Nature* **324**, 361–364. (doi:10.1038/324361a0)
25. Narayan SM, Santori EM, Toga AW. 1994 Mapping functional activity in rodent cortex using optical intrinsic signals. *Cereb. Cortex* **4**, 195–204. (doi:10.1093/cercor/4.2.195)
26. Holtmaat A *et al.* 2009 Long-term, high-resolution imaging in the mouse neocortex through a chronic cranial window. *Nat. Protoc*. **4**, 1128–1144. (doi:10.1038/nprot.2009.89)
27. Shih AY, Mateo C, Drew PJ, Tsai PS, Kleinfeld D. 2012 A polished and reinforced thinned skull window for long-term imaging and optical manipulation of the mouse cortex. *J. Vis. Exp*. **67**, e3742. See http://www.jove.com/video/3742.
28. Drew PJ, Shih AY, Driscoll JD, Knutsen PM, Davalos D, Blinder P, Akassoglou K, Tsai PS, Kleinfeld D. 2010 Chronic optical access through a polished and reinforced thinned skull. *Nat. Methods* **7**, 981–984. (doi:10.1038/nmeth.1530)
29. Ogawa S, Lee T-M, Nayak AS, Glynn P. 1990 Oxygenation-sensitive contrast in magnetic resonance image of rodent brain at high fields. *Magn. Reson. Med*. **14**, 68–78. (doi:10.1002/mrm.1910140108)
30. Ogawa S, Lee TM. 1990 Magnetic resonance imaging of blood vessels at high fields: *in vivo* and *in vitro* measurements and image simulation. *Magn. Reson. Med*. **16**, 9–18. (doi:10.1002/mrm.1910160103)
31. Pauling L, Coryell CD. 1936 The magnetic properties and structure of hemoglobin, oxyhemoglobin and carbonmonoxyhemoglobin. *Proc. Natl Acad. Sci. USA* **22**, 210–216. (doi:10.1073/pnas.22.4.210)
32. Devor A, Dunn AK, Andermann ML, Ulbert I, Boas DA, Dale AM. 2003 Coupling of total hemoglobin concentration, oxygenation, and neural activity in rat somatosensory cortex. *Neuron* **39**, 353–359. (doi:10.1016/S0896-6273(03)00403-3)
33. Hillman EMC. 2007 Optical brain imaging *in vivo*: techniques and applications from animal to man. *J. Biomed. Opt*. **12**, 051402. (doi:10.1117/1.2789693)
34. Boas DA, Dale AM, Franceschini MA. 2004 Diffuse optical imaging of brain activation: approaches to optimizing image sensitivity, resolution, and accuracy. *Neuroimage* **23**, S275–S288. (doi:10.1016/j.neuroimage.2004.07.011)
35. Chen-Bee CH, Agoncillo T, Xiong Y, Frostig RD. 2007 The triphasic intrinsic signal: implications for functional imaging. *J. Neurosci*. **27**, 4572–4586. (doi:10.1523/JNEUROSCI.0326-07.2007)
36. Drew PJ, Shih AY, Kleinfeld D. 2011 Fluctuating and sensory-induced vasodynamics in rodent cortex extends arteriole capacity. *Proc. Natl Acad. Sci. USA* **108**, 8473–8478. (doi:10.1073/pnas.1100428108)
37. Devor A *et al.* 2007 Suppressed neuronal activity and concurrent arteriolar vasoconstriction may explain negative blood oxygenation level-dependent signaling. *J. Neurosci*. **27**, 4452–4459. (doi:10.1523/JNEUROSCI.0134-07.2007)
38. Zong X, Kim T, Kim S-G. 2012 Contributions of dynamic venous blood volume versus oxygenation level changes to BOLD fMRI. *Neuroimage* **60**, 2238–2246. (doi:10.1016/j.neuroimage.2012.02.052)
39. Berwick J, Johnston D, Jones M, Martindale J, Martin C, Kennerley AJ, Redgrave P, Mayhew JE. 2008 Fine detail of neurovascular coupling revealed by spatiotemporal analysis of the hemodynamic response to single whisker stimulation in rat barrel cortex. *J. Neurophysiol*. **99**, 787–798. (doi:10.1152/jn.00658.2007)
40. Frostig RD, Dory Y, Kwon MC, Masino SA. 1993 Characterization of functional organization within rat barrel cortex using intrinsic signal optical imaging through a thinned skull. *Proc. Natl Acad. Sci. USA* **90**, 9998–10002. (doi:10.1073/pnas.90.21.9998)

41. Sheth BR, Moore I, Sur M. 1998 Temporal modulation of spatial borders in rat barrel cortex. *J. Neurophysiol*. **79**, 464–470.
42. Prakash N, Vanderhaeghen P, Cohen-Cory S, Frisen J, Flanagan JG, Frostig RD. 2000 Malformation of the functional organization of somatosensory cortex in adult ephrin-A5 knock-out mice revealed by *in vivo* functional imaging. *J. Neurosci*. **20**, 5841–5847.
43. Vazquez AL, Fukuda M, Kim SG. 2012 Evolution of the dynamic changes in functional cerebral oxidative metabolism from tissue mitochondria to blood oxygen. *J. Cereb. Blood Flow Metab*. **32**, 745–758. (doi:10.1038/jcbfm.2011.198)
44. Shtoyerman E, Arieli A, Slovin H, Vanzetta I, Grinvald A. 2000 Long-term optical imaging and spectroscopy reveal mechanisms underlying the intrinsic signal and stability of cortical maps in V1 of behaving monkeys. *J. Neurosci*. **20**, 8111–8121.
45. Desai M *et al.* 2011 Mapping brain networks in awake mice using combined optical neural control and fMRI. *J. Neurophysiol*. **105**, 1393–1405. (doi:10.1152/jn.00828.2010)
46. Berwick J, Martin C, Martindale J, Jones M, Johnston D, Zheng Y, Redgrave P, Mayhew J. 2002 Hemodynamic response in the unanesthetized rat: intrinsic optical imaging and spectroscopy of the barrel cortex. *J. Cereb. Blood Flow Metab*. **33**, 670–679. (doi:10.1097/00004647-200206000-00005)
47. Chen LM. 2005 Optical imaging of SI topography in anesthetized and awake squirrel monkeys. *J. Neurosci*. **25**, 7648–7659. (doi:10.1523/JNEUROSCI.1990-05.2005)
48. Marcar VL, Schwarz U, Martin E, Loenneker T. 2006 How depth of anesthesia influences the blood oxygenation level-dependent signal from the visual cortex of children. *Am. J. Neuroradiol*. **27**, 799–805.
49. Martin C, Martindale J, Berwick J, Mayhew J. 2006 Investigating neural–hemodynamic coupling and the hemodynamic response function in the awake rat. *Neuroimage* **32**, 33–48. (doi:10.1016/j.neuroimage.2006.02.021)
50. Goense JBM, Logothetis NK. 2008 Neurophysiology of the BOLD fMRI signal in awake monkeys. *Curr. Biol*. **18**, 631–640. (doi:10.1016/j.cub.2008.03.054)
51. Pisauro MA, Dhruv NT, Carandini M, Benucci A. 2013 Fast hemodynamic responses in the visual cortex of the awake mouse. *J. Neurosci*. **33**, 18 343–18 351. (doi:10.1523/JNEUROSCI.2130-13.2013)
52. Qiu M, Ramani R, Swetye M, Rajeevan N, Constable RT. 2008 Anesthetic effects on regional CBF, BOLD, and the coupling between task-induced changes in CBF and BOLD: an fMRI study in normal human subjects. *Magn. Reson. Med*. **60**, 987–996. (doi:10.1002/mrm.21759)
53. Iida H, Ohata H, Iida M, Watanabe Y, Dohi SI. 1998 Isoflurane and sevoflurane induce vasodilation of cerebral vessels via ATP-sensitive $K^+$ channel activation. *Anesthesiology* **89**, 954–960. (doi:10.1097/00000542-199810000-00020)
54. Kim T, Kim SG. 2011 Temporal dynamics and spatial specificity of aterial and venous blood volume changes during visual stimulation: implication for BOLD quantification. *J. Cereb. Blood Flow Metab*. **31**, 1211–1222. (doi:10.1038/jcbfm.2010.226)
55. Fukuda M, Wang P, Moon C-H, Tanifuji M, Kim S-G. 2006 Spatial specificity of the enhanced dip inherently induced by prolonged oxygen consumption in cat visual cortex: implication for columnar resolution functional MRI. *Neuroimage* **30**, 70–87. (doi:10.1016/j.neuroimage.2005.09.026)
56. Arenkiel BR, Peca J, Davison IG, Feliciano C, Deisseroth K, Augustine GJ, Ehlers MD, Feng G. 2007 *In vivo* light-induced activation of neural circuitry in transgenic mice expressing channelrhodopsin-2. *Neuron* **54**, 205–218. (doi:10.1016/j.neuron.2007.03.005)
57. Babbitt JT, Kharazi AI, Taylor JMG, Bonds CB, Zhuang D, Mirell SG, Frumkin E, Hahn T. 2001 Increased body weight in C57BL/6 female mice after exposure to ionizing radiation or 60 Hz magnetic fields. *Int. J. Radiat. Biol*. **77**, 875–882. (doi:10.1080/09553000110055790)
58. Shih AY, Driscoll JD, Drew PJ, Nishimura N, Schaffer CB, Kleinfeld D. 2012 Two-photon microscopy as a tool to study blood flow and neurovascular coupling in the rodent brain. *J. Cereb. Blood Flow Metab*. **32**, 1277–1309. (doi:10.1038/jcbfm.2011.196)
59. Kohn A, Metz C, Quibrera M, Tommerdahl MA, Whitsel BL. 2000 Functional neocortical microcircuitry demonstrated with intrinsic signal optical imaging *in vitro*. *Neuroscience* **95**, 51–62. (doi:10.1016/S0306-4522(99)00385-1)
60. Akrawi WP, Drummond JC, Kalkman CJMPP. 1996 A comparison of the electrophysiologic characteristics of EEG burst-suppression as produced by isoflurane, thiopental, etomidate, and propofol. *J. Neurosurg. Anesthesiol*. **8**, 40–46. (doi:10.1097/00008506-199601000-00010)
61. Nagaoka T, Zhao F, Wang P, Harel N, Kennan RP, Ogawa S, Kim SG. 2005 Increases in oxygen consumption without cerebral blood volume change during visual stimulation under hypotension condition. *J. Cereb. Blood Flow Metab.* **26**, 1043–1051. (doi:10.1038/sj.jcbfm.96000251)
62. Welker E, Van der Loos H. 1986 Quantitative correlation between barrel-field size and the sensory innervation of the whiskerpad: a comparative study in six strains of mice bred for different patterns of mystacial vibrissae. *J. Neurosci*. **6**, 3355–3373.
63. Egger R, Narayanan RT, Helmstaedter M, de Kock CPJ. 2012 3D reconstruction and standardization of the rat vibrissal cortex for precise registration of single neuron morphology. *PLoS Comput. Biol*. **8**, e1002837. (doi:10.1371/journal.pcbi.1002837)
64. Kleinfeld D, Deschênes M. 2011 Neuronal basis for object location in the vibrissa scanning sensorimotor system. *Neuron* **72**, 455–468. (doi:10.1016/j.neuron.2011.10.009)
65. Felleman DJ, Van Essen DC. 1991 Distributed hierarchical processing in the primate cerebral cortex. *Cereb. Cortex* **1**, 1–47. (doi:10.1093/cercor/1.1.1)
66. Wang Q, Burkhalter A. 2007 Area map of mouse visual cortex. *J. Comp. Neurol*. **502**, 339–357. (doi:10.1002/cne.21286)
67. Reale RA, Imig TJ. 1980 Tonotopic organization in auditory cortex of the cat. *J. Comp. Neurol*. **192**, 265–291. (doi:10.1002/cne.901920207)
68. Langner GM, Sams M, Heil P, Schulze H. 1997 Frequency and periodicity are represented in orthogonal maps in the human auditory cortex: evidence from magnetoencephalography. *J. Comp. Physiol. A* **181**, 665–676. (doi:10.1007/s003590050148)
69. Stiebler I, Neulist R, Fichtel I, Ehret G. 1997 The auditory cortex of the house mouse: left–right differences, tonotopic organization and quantitative analysis of frequency representation. *J. Comp. Physiol. A* **181**, 559–571. (doi:10.1007/s003590050140)